On the Optimization of Roughness and Corrosion Resistance of Laser Beam Powder Bed Fusion Fabricated Ti–6Al–4V Parts—An Electrochemical Approach

Shamim Pourrahimi and Lucas A. Hof*

Laser beam powder bed fusion is emerging as a technology for fabricating components made of advanced alloys, such as Ti–6Al–4V. However, it suffers from rough as-built (AB) surfaces, necessitating postprocessing for desired quality and performance. Electrochemical methods such as electrochemical polishing (ECP) and anodization (AN) are promising postprocessing methods; ECP can effectively smoothen surfaces irrespective of their complexity and hardness, while AN enhances the material's corrosion resistance. However, literature lacks research that discusses combined ECP and AN treatment on surface texture evaluation and corrosion behavior. This work presents a detailed study on the effects of different processing factor levels using a Taguchi design of experiment (DOE) approach and discusses the underlying process mechanisms. The optimized treatment conditions to achieve highest roughness improvement and best corrosion resistance are discussed and the most influential postprocessing factors are revealed and ranked. The treatment that achieved smooth surfaces and high corrosion resistance is ECP at 20 V and 15 °C for 20 min, followed by AN at 15 V for 5 min. This treatment achieves a 72% roughness improvement, providing an arithmetic areal surface roughness of 2.63 µm and a corrosion current density of 0.09 µA cm^{-2}, which is almost similar to the AB part.

1. Introduction

Titanium and its alloys have been widely used in biomedical,[1] aerospace,[2] marine,[3] and automotive industries,[4] due to their high strength, chemical resistance, and biocompatibility. These industries often require complex or custom-designed parts that are difficult to produce using traditional manufacturing methods. In such cases, additive manufacturing (AM) emerges as a favorable alternative. AM is a rapidly advancing technology that builds components in a layer-by-layer process, which allows for the fabrication of complex geometries and customized designs that would be challenging or impossible to create with conventional methods.[5–8] This approach also enables significant material savings and reduces lead times, making it ideal for applications where rapid prototyping or small-batch production is required.[9]

Among the various AM methods, laser beam powder bed fusion (PBF-LB) is widely used for producing metallic parts.[10] PBF-LB is a subset of powder bed fusion (PBF) processes, which involves spreading a thin layer of metal powder (typically 20–100 µm) over a build plate and selectively melting specific areas using a focused energy source, such as a laser beam. This process is repeated layer by layer until the final component is constructed.[11] One of the distinctive features of PBF-LB is the high cooling rate that occurs after the laser energy melts the material. These fast cooling rates can lead to unique microstructures with desirable mechanical properties but my also introduce residual stress due to the rapid solidification.[9,11]

However, PBF-LB parts typically exhibit inferior surface quality compared to those produced using conventional manufacturing methods, such as machining.[11] This is primarily attributed to the layer-by-layer nature of AM and the physical phenomena that occur during the deposition and fusion of the feedstock. This process can result in highly irregular surface features and the formation of semimelted particles on the surface, as well as a characteristic staircase effect due to the discrete layering.[12] Additionally, the high energy input required to melt the powder can cause overheating of areas adjacent to the melt zone, further contributing to surface irregularities.[11,13] In addition, the layer-by-layer deposition and melting result in a distinct texture to the surface parallel to the build direction, known as the staircase effect.[14] Despite these challenges, PBF-LB remains an attractive manufacturing method due to its versatility in producing complex geometries and the potential for tailored material properties through process parameter control.[15]

These rough surfaces of parts produced by AM present several disadvantages. First, the aesthetic appeal of the part may be compromised, affecting its overall quality perception.[16] Second, the rough surface increases friction and wear, potentially reducing

S. Pourrahimi, L. A. Hof
Mechanical Engineering Department
École de technologie supérieure
1100, rue Notre-Dame Ouest, Montréal, Québec H3C 1K3, Canada
E-mail: lucas.hof@etsmtl.ca

The ORCID identification number(s) for the author(s) of this article can be found under https://doi.org/10.1002/adem.202401395.

the component's lifespan.[17] Additionally, stress concentration points can form on rough surfaces, weakening the structural integrity of the part.[18] Moreover, the rough surface can accelerate corrosion, making the part more susceptible to degradation in corrosive environments.[19] Finally, rough surfaces disrupt fluid flow, leading to increased turbulence and reduced efficiency in applications involving fluid dynamics.[20,21] Therefore, it is important to effectively control the surface roughness of AM parts to ensure their optimal performance in their intended applications.

Effective parameters in the PBF-LB process, such as feed stock properties, layer thickness,[11] hatching,[22] laser power, scanning speed, and building direction[23] may control the surface quality of the as-built (AB) part. However, for most applications, further postprocessing is required to meet the fabricated part's service conditions.

In general, postprocessing techniques can be categorized into four main groups: 1) mechanical (abrasive); 2) laser; 3) chemical; and 4) electrochemical methods. The selection of the appropriate method depends on multiple factors, such as the material properties, part geometry, complexity, and desired level of finishing.[12,24] Each of the postprocessing methods offers its own advantages and suitability based on these considerations. The present study specifically investigates electrochemical polishing (ECP) as a technique that provides significant advantages. One notable advantage is its capability to access and treat intricate internal surfaces, regardless of their hardness.[25,26] As well, ECP enables efficient material removal and surface refinement in complex areas that are typically challenging to reach using alternative polishing methods.[24]

As per the definition provided by the ASTM B374 standard, ECP is a method that enhances the surface finish of a metal by making the metallic part anodic within a suitable solution.[27] The process is driven by electrochemical oxidation, where the metal surface acts as the anode in an electrolytic cell. When an electrical potential is applied, metal atoms at the surface oxidize and dissolve into the electrolyte as ions. Due to the higher current density at surface asperities, these areas dissolve more quickly than the smoother regions, resulting in a leveled and polished surface. This specific dissolution mechanism makes ECP effective in smoothing metallic surfaces, regardless of their hardness. However, while ECP can be applied to complex parts, it requires careful consideration of the process parameters. In particular, ensuring consistent electrolyte flow and ion exchange can be challenging in complex geometries, such as internal holes with intricate helical shapes.[28,29]

This process can be manipulated by various factors, including potential and/or current density, temperature, time, electrolyte composition, electrode working distance, electrolyte flow, and other relevant parameters. However, it is still difficult to meet the industrial standards and requirements for part finishing by ECP, specifically in the biomedical industry.[30] By adjusting the ECP factors, this process can be effectively controlled to achieve the desired surface finish on the metal part.[31] Literature suggests that, typically, good surface finish can be achieved, when ECP is performed in the potential/current density range within the workpiece-electrolyte system polarization curves' limiting current plateau region.[25] However, such plateau does not exist for all metals including Ti alloys. Wu et al.[32]

observed that there was no plateau in the current density versus potential curve when polarizing an additive-manufactured Ti–6Al–4V part in the potential range of 0–24 V.
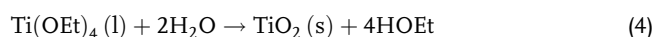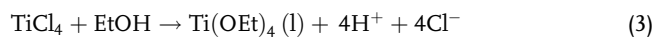
Due to the mass-controlled nature of ECP, temperature has a significant impact on the process. Generally, higher temperatures result in accelerated diffusion of dissolved metal and acceptor ions, increased ion solubility, reduced electrolyte viscosity, and a thinner viscous layer on the electrolyte.[31,33] Nevertheless, excessively raising the temperature is not beneficial, as it can lead to the emergence of defects such as pitting on the sample's surface.[28,34]

ECP time is another critical factor influencing the part's final roughness and mass loss. Experimental findings demonstrate an exponential decrease in surface roughness as the polishing time increases.[35] In general, a longer duration of ECP leads to a smoother surface. However, it is important to consider other factors such as manufacturing time, control over mass loss, and the avoidance of significant changes in geometry, i.e., for near-net-shape manufacturing. Therefore, it is necessary to carefully control the ECP time to achieve the desired surface quality, while maintaining control over these end-application important aspects.

The electrolyte used in ECP serves as a carrier for current, heat, and reaction products. Indeed, the concentration of reacting ions in the electrolyte directly influences the dissolution of the metallic material during the process.[36] In the past decades, toxic, acidic, and aggressive electrolytes were commonly used for the ECP of titanium alloys;[37,38] however, in recent years, there has been a shift toward more environmentally friendly approaches. Nonaqueous electrolytes, consisting of organic solvents like ethylene glycol or propylene combined with sodium chloride (NaCl) and ethanol, have shown promising results in ECP of titanium alloys.[39,40] Regarding the mechanism of Ti dissolution in such an eco-friendly electrolyte, Kim et al.[39] highlighted the role of added ethanol to the ethylene glycol and NaCl solution. According to their study, ethylene glycol contains traces of water as an impurity. Once the ECP begins and an overpotential is applied to the part, $TiCl_4$ is formed, as described by Equation (1). Then, in a second step, due to the presence of water in the electrolyte, titanium dioxide (TiO_2) is formed on the surface, as presented by Equation (2):

$$Ti^{4+} + 4\,Cl^- \rightarrow TiCl_4\,(l) \tag{1}$$

$$TiCl_4\,(l) + 2H_2O \rightarrow TiO_2\,(s) + 4H^+ + 4Cl^- \tag{2}$$
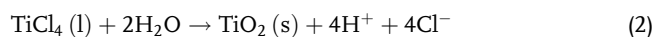
In the context of ECP, the goal is material dissolution, while the material oxidizes. However, the formed TiO_2 does not dissolve in the electrolyte and instead accumulates on the surface, hindering further material dissolution, which is not ideal for ECP. Therefore, as suggested in this study, the addition of ethanol helps the dissolved $TiCl_4$ to react with water molecules via the added ethanol (Et), as described in Equation (3) and (4), away from the electrodes.[39]

$$TiCl_4 + EtOH \rightarrow Ti(OEt)_4\,(l) + 4H^+ + 4Cl^- \tag{3}$$

$$Ti(OEt)_4\,(l) + 2H_2O \rightarrow TiO_2\,(s) + 4HOEt \tag{4}$$

Other important factors that impact the ECP process include the electrode distance and electrolyte flow. In fact, they have a significant influence on the kinetic behavior of the electrochemical cell, affecting the workpiece's final surface roughness and mass removal rate. Therefore, it is necessary to carefully consider and select appropriate values for both electrode distance and electrolyte flow to achieve desired outcomes in terms of surface quality and material removal, which is still a challenging task.[31]

Despite the superior chemical resistivity of Ti alloys, it is important to consider that there can be situations where corrosion-related issues occur.[41] This is particularly crucial when considering the application of AM Ti alloys in environments that are susceptible to corrosion, such as marine or biomedical applications. One significant concern is the potential release of ions from the alloy, which can have detrimental effects on biological tissue in medical applications.[42] Additionally, the occurrence of pitting corrosion poses a notable risk as it can cause localized damage to the material, ultimately leading to part failure.[43]

Controlling the passive film formation is important to enhance the corrosion behavior of Ti alloys. Electrochemical anodization (AN), also known as anodic oxidation, is a widely used technique to create a stable and protective TiO_2 layer. Unlike the natural oxide layer formed in ambient conditions, the oxide layer produced by AN is significantly thicker, more uniform, and strongly adherent, which contributes to the material's enhanced resistance to corrosion in aggressive environments.[44] Similar to ECP, during AN, a constant current or potential is applied to the part immersed in a conductive electrolyte.[45] When ECP is performed in an ethanol-containing electrolyte, no TiO_2 forms on the surface. Hence, by introducing a subsequent AN treatment, a protective TiO_2 can be formed on the surface to improve the corrosion resistivity.[44] The mixture of NaCl and ethylene glycol can be used for AN as an eco-friendly solution. However, to promote the formation of oxides rather than material dissolution, a higher water content and lower NaCl concentration should be used.[46] Nguyen et al. proposed the use of a 0.3 M NaCl solution in a mixture of 50 vol% ethylene glycol and 50 vol% water.[47]

Rodríguez-Martínez et al.[48] investigated the quality of the TiO_2 passive film formed on pure Ti foil using ECP and AN methods. They observed the formation of vertically oriented TiO_2 nanotubes on electropolished surfaces, but the corrosion resistivity was not measured. In another study by Zhang et al.[36] a decrease in the corrosion current density of AM Ti–6Al–4V alloy was reported after ECP in a solution of 0.2 M $MgCl_2$ + ethylene glycol. The observed increase in corrosion resistance in this reported study[36] may be related to the formation of TiO_2, since their electrolyte did not contain ethanol. However, according to the proposed mechanisms of Ti dissolution, ethanol is necessary for an efficient ECP treatment.[39] In fact, literature lacks studies that evaluate the corrosion properties of Ti alloy parts after ECP in an electrolyte which avoids TiO_2 formation. As well, studies that examine a subsequent—post-ECP—AN step that can affect the corrosion resistance are absent in literature.

The objective of this study is to examine the effects of various combinations of ECP potential, temperature, and time on surface roughness enhancement and material removal rate (MRR) to optimize these ECP parameters for surface roughness and corrosion resistance improvement. Additionally, to assess the influence of AN on corrosion behavior of AM parts, AN experiments were conducted following ECP, varying the potential and duration as controlled parameters. Among the available electrolytes recommended for postprocessing of Ti alloy, this study has prioritized an ethylene glycol-based solution due to its eco-friendliness compared to acidic alternatives. It is worth mentioning that additional factors such as electrolyte composition, flow rate, and working distance can also influence the ECP process. However, for the purpose of this study, these variables were held constant and their specific impact will not be extensively discussed, as this topic is already well-documented in literature.[35,39] Hence, the selected values for these parameters are based on literature combined with preliminary validation experiments.

2. Experimental Section

In this section, a detailed explanation of the experimental procedure is presented. This includes the materials and solutions in Section 2.1, the ECP and AN procedure in Section 2.2, and the sample characterization methods, which are presented in Section 2.3. Section 2.3 is further divided into three subsections: Section 2.3.1 for roughness measurement, Section 2.3.2 for mass measurement, and Section 2.3.3 for corrosion measurement. Finally, Section 2.4 outlines the DOEs approach used for optimization. **Figure 1** summarizes the overview of the experimental procedure used in this study, and the details will be elaborated in the subsequent subsections.
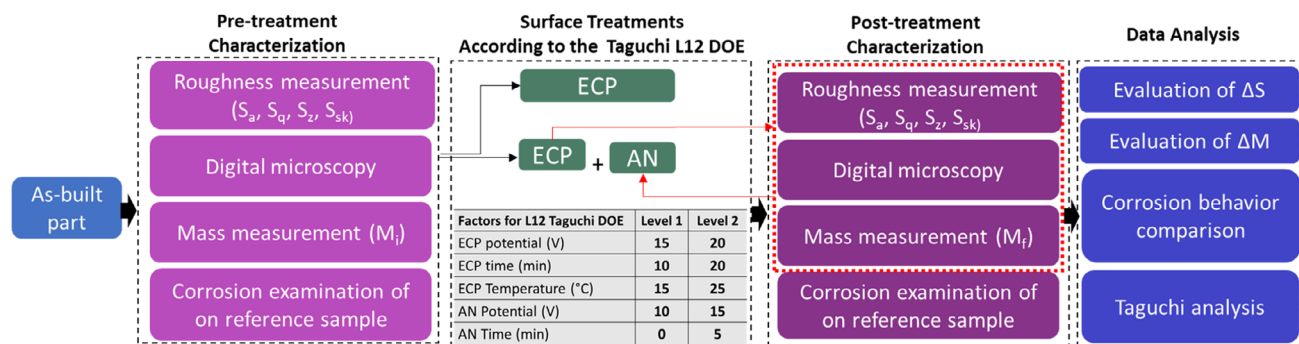

Figure 1. Schematic of methodology and experimental procedure to find optimal surface treatment of the Ti–6Al–4V AM parts.

2.1. Materials and Solutions

For this study, the samples, presented in **Figure 2**a, were produced using PBF-LB technology, employing a plasma-atomized Ti–6Al–4V powder with diameters within the 15–45 μm range. The chemical composition of the Ti–6Al–4V powder used for sample fabrication by PBF-LB is according to the requirements specified in ASTM F136[49] and is provided in **Table 1**.

To conduct the ECP treatment, an eco-friendly electrolyte solution was prepared following the method suggested by Kim et al.[39] Ethylene glycol (Certified, 99.8% pure with a maximum water content of 0.2%, Fisher Chemical) was mixed with sodium chloride (analytical grade, Fisher Chemical) to create a 1 M NaCl solution. Subsequently, 20 vol% ethanol (99.9%+, Fisher Chemicals) was added to the mixture.

For the AN step following ECP, a solution of 0.3 M NaCl in a mixture of 50 vol% ethylene glycol/water was used according to other reported studies on the AN of titanium alloys.[47,48]

To perform electrochemical corrosion measurements, a 3.5 wt% NaCl solution was utilized as the electrolyte, which is commonly used as an electrolyte in corrosion experiments. This concentration closely resembles seawater and water in marine environments; however, it exhibits a slightly higher level of corrosive aggressiveness.[50]

2.2. Electrochemical Polishing and AN Methods

Figure 3 illustrates a schematic representation of the deployed three-electrode ECP cell. The working electrode (WE) functions as the anode and represents the workpiece that undergoes polishing. The counter electrode (CE) acts as the cathode and completes the electric circuit to enable the current flow. A stainless steel 316L sheet, abraded using 1200-grit abrasive paper, was used as CE. The reference electrode (RE), a silver-silver chloride (Ag/AgCl) was the reference electrode (0.209 V vs standard hydrogen electrode), allows for the measurement of the potential in close proximity to the WE, minimizing the disruptive effects caused by factors like electrode polarization and electrolyte resistance, which dynamically fluctuate during the ECP process.

Table 1. Chemical composition of the virgin Ti–6Al–4V powder (wt%).

	Al	V	Fe	O	C	N	H	Ti
Powder	6.25	4.0	0.22	0.10	0.01	0.01	0.002	Balance

To ensure a consistent temperature throughout the process, a double-walled cell and a Cole-Parmer Polystat heating/cooling circulating bath equipped with a thermostat were employed for water circulation at controlled temperature. Additionally, to eliminate the agglomeration of reaction's products on the surface and facilitate access of fresh electrolyte to the electrodes, magnetic stirring at a speed of 200 rpm was utilized. A BK PRECISION 9117 power supply was used to apply the potential for the treatments. A dedicated LabVIEW program was developed and employed to regulate the potential difference between the RE and the WE, ensuring the consistent application of potential between the WE and CE throughout the electrochemical treatment, hence acting as potentiostat.

AN was performed using the same cell and setup but using a different electrolyte and potential range. For all ECP and AN treatments, as shown in Figure 2b, a square shape surface area ($0.55–0.60 \text{ cm}^2$) was exposed to the electrolyte for corrosion characterization. The rest of the parts were insulated with electrical insulator paints.

2.3. Sample Characterization Methods

The treated samples are analyzed through three distinct methods: surface roughness measurement (Section 2.3.1), mass measurement (Section 2.3.2), and corrosion examination (Section 2.3.3). Each method is comprehensively described in its respective subsection.

2.3.1. Roughness Measurement

Surface roughness measurement serves as a means to assess the effectiveness of surface treatments. While the arithmetic average roughness (R_a) is the commonly utilized parameter in this
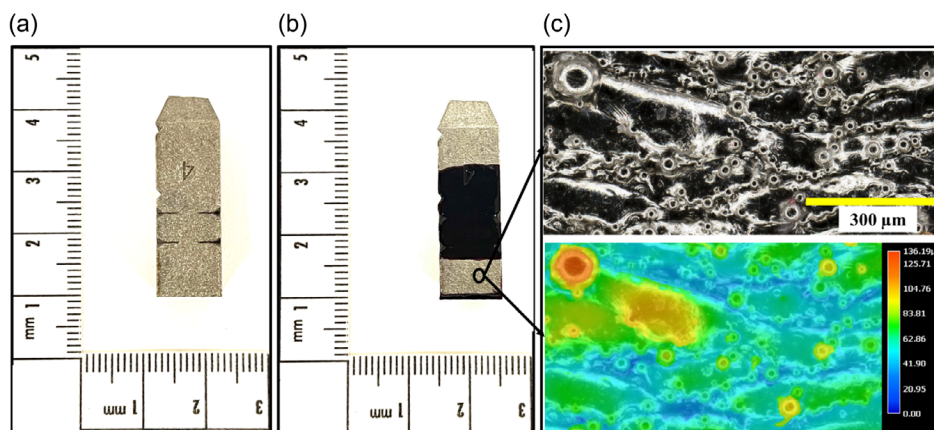

Figure 2. a) Photograph of the PBF-LB produced Ti–6Al–4V sample utilized in the study; b) the sample postapplication of electrical insulator coating for corrosion testing; and c) digital microscope image alongside the color map representation of the AB surface.
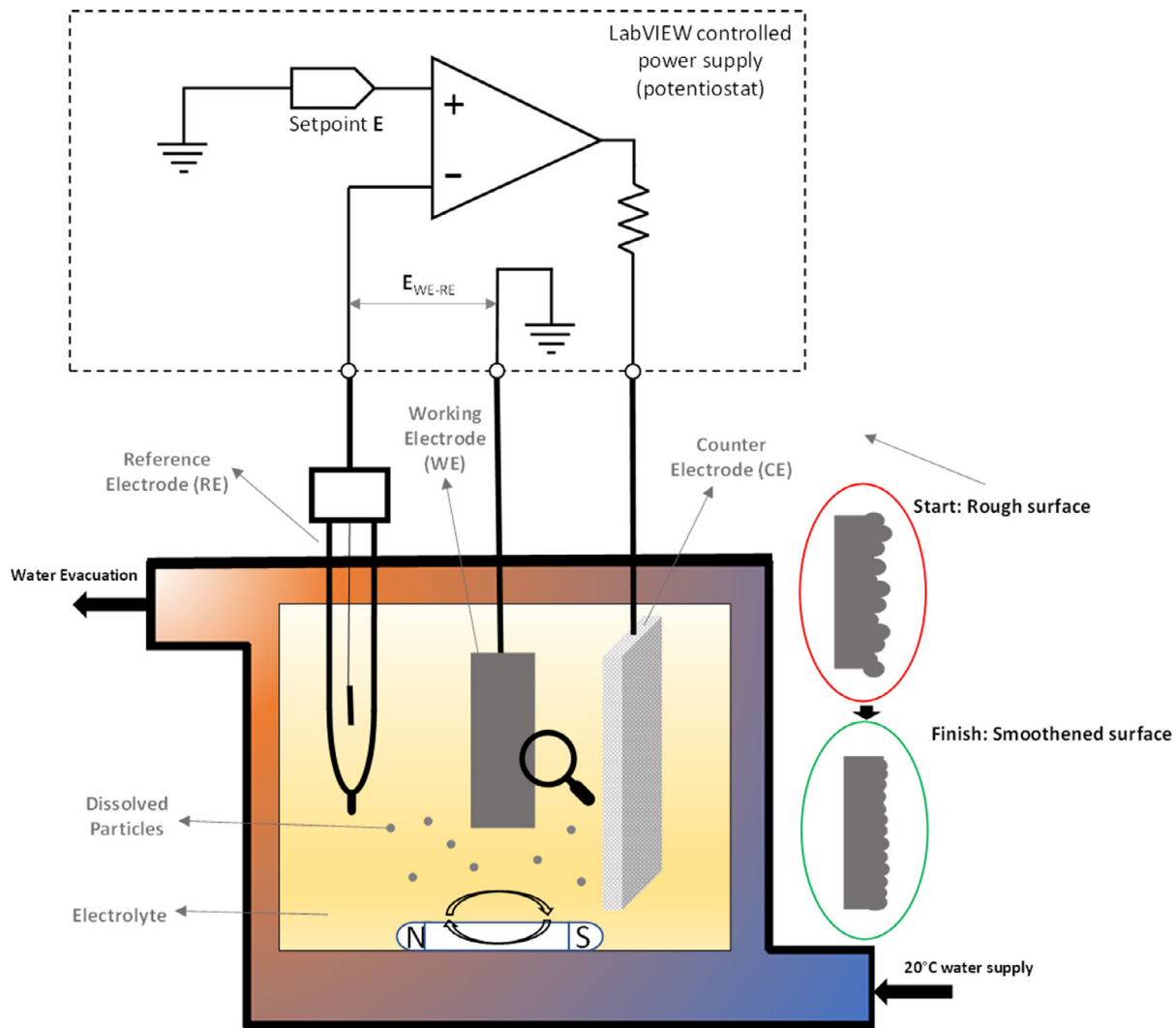
**ADVANCED
SCIENCE NEWS**

www.advancedsciencenews.com

**ADVANCED
ENGINEERING
MATERIALS**

www.aem-journal.com

Figure 3. Schematic of a three-electrode system used for ECP and AN surface treatments with an integrated home-built LabVIEW control system including a power supply, depicted in the dashed square.

context,[51–53] it provides only limited insights into surface topography since it is conducted along a single line.[54] Alternatively, areal roughness measurements can be employed to describe the surface texture in a three-dimensional space.[8,21] Hence, according to the recommendation of standard ASTM F3624-23,[55] the arithmetic mean height of areal surface roughness (S_a), the root mean square height (S_q), the sum of the maximum peak height and the maximum valley depth values (S_z), and the skewness of surface heights (S_{sk}), which is the quotient of the mean cube value of the ordinate values and the cube of S_q, were chosen for this study to evaluate the improvement in roughness achieved through the ECP process.[24]

The surface texture measurement was conducted in accordance with ISO 25178 standards using a Keyence digital microscope model VHX-7000. The measurement covered a stitched surface area of 3×3 mm obtained with a 1000X lens. Roughness calculations were performed using the microscope

software, employing a scale-limited surface (S-L) filter with prior tilt correction. According to the ASTM F3624-23 standard, considering a minimum surface area of 2.5×2.5 mm is sufficient for surface texture studies of AM parts. A laser confocal microscope, LEXT 4100 (Olympus), and scanning electron microscopy (SEM) using a Hitachi SU-70 field emission electron microscope were used to examine the localized defects after processing and corrosion examinations.

2.3.2. Mass Measurement

Mass measurements were conducted both before and after each ECP treatment, utilizing a digital laboratory balance, with the resolution of 0.0001, from SARTORIUS. These measurements were repeated five times, and the resulting averages were employed for the calculation of the MRR.

**ADVANCED
SCIENCE NEWS**

www.advancedsciencenews.com

**ADVANCED
ENGINEERING
MATERIALS**

www.aem-journal.com

2.3.3. Corrosion Examination

Electrochemical measurements were carried out in a three-electrode cell connected to a Metrohm Autolab PGSTAT 302 N potentiostat. The experiments were conducted in a double-walled glass cell with multiple inlets for electrodes and water circulation to control the temperature. In the three-electrode system, Ag/AgCl was the RE, a coiled platinum wire (99.99% pure) was used as the CE, and the AM Ti–6Al–4V part was mounted as the WE. The corrosion behavior of the part was investigated using the potentiodynamic polarization technique[56] To ensure electrochemical stability before commencing the corrosion test, the open circuit potential (OCP) was monitored for 20 min. Subsequently, the WE was polarized within the range of -0.4 to $+6.0\,V$ versus OCP, with a scan rate of $50\,mV\,s^{-1}$.

2.4. DOE

DOE is an effective method for identifying critical factors and determining optimal conditions in today's industrial processes.[57] The present study utilized the Taguchi method, which employs orthogonal arrays to systematically evaluate the factors and their levels influencing the ECP and AN process. Unlike the full factorial method, which requires testing of all possible combinations, the Taguchi method examines pairs of combinations to minimize the number of trials needed.[58]

In this study, a L12 array has been generated, encompassing five factors, each including two levels. This array is chosen to take advantage of its capability to investigate the main effects of each factor independently.[59] Here, the factors comprise ECP potential, time, temperature, as well as AN potential and time, and their respective levels, based on values reported in literature for similar environments and preliminary experiments, are specified in **Table 2**. In a previous study conducted by the authors,[29] preliminary experiments showed that a single ECP treatment reduced the corrosion resistance of the Ti–6Al–4V parts. One of the present study objectives is to systematically evaluate the

possibility and effectiveness of an added AN step to form an oxide layer that improves the corrosion behavior after ECP treatment. The AN potentials and times were selected based on the study by Rodríguez-Martínez et al.[48] which used a similar electrolyte for anodizing Ti foils. Additionally, preliminary experiments were performed to ensure that the selected parameters would be effective for Ti–6Al–4V AM parts. To ensure the repeatability of the results, each experiment was conducted three times.

Regarding the AN time, it should be highlighted that two levels, including 0 and 5 min are considered. Indeed, when we refer to 0 min, it means that no AN treatment is performed. This is done to evaluate how the corrosion behavior changes between the only ECP-treated samples and the ECP + AN-treated samples.

It is important to mention that in the L12 orthogonal array used for this study, some experiments may appear identical when fewer than six factors are included. This is a known characteristic of the Taguchi design methodology and is mathematically consistent with the principles of orthogonal arrays. Despite the repetition, the Taguchi analysis remains valid and allows for a robust investigation of the factors under study.[59]

These factors and levels are chosen to investigate their influence on roughness improvement, MRR, and corrosion behavior. This study uses Taguchi analysis of means to identify the most important factors contributing to the process. According to Equation (5), the means of responses (γ_{mean}), i.e., roughness improvement, MRR, and corrosion current density, are the average of responses of the specific level of specific factors:

$$\gamma_{mean} = \left(\sum_{i=1}^{n} \gamma_i \right) \Big/ n \tag{5}$$

where γ_i is the output under observation and n is the number of experiments.

Equation (6) and (7) are used to calculate the roughness changes and the MRR for each experimental set:

$$\Delta S = |\text{Final roughness} - \text{Initial roughness}| \tag{6}$$

$$MRR = \frac{\Delta M}{t} = \frac{(M_i - M_f)}{t} \tag{7}$$

where ΔS represents the absolute change in the areal roughness value parameter (S_a, S_q, S_z, or S_{sk}) due to ECP treatment. In Equation (7), ΔM is the mass change by the ECP treatment, M_i is the mass of the sample before treatment, expressed in mg, M_f is the mass after treatment (mg), and t is the processing time expressed in minutes. The corrosion rate is calculated using the Tafel equation (Equation 8):

$$E - E_{corr} = a \pm b \log|i| \tag{8}$$

where E is the applied potential, E_{corr} is corrosion potential, a and b denote the Tafel constant and slope, respectively, the "$\pm$" sign indicates in which domain the sample operates ("$+$" for the anodic domain and "$-$" for the cathodic domain), and i denotes the current density.

Table 2. L12 orthogonal array Taguchi DOE for ECP and AN of AM Ti–6Al–4V parts.

Experiment # (sample)	ECP potential [V]	ECP time [min]	ECP temperature [°C]	AN potential [V]	AN time [min]
Experiment#1 (S1)	15	10	15	15	0
Experiment#2 (S2)	15	10	15	15	0
Experiment#3 (S3)	15	10	25	10	5
Experiment#4 (S4)	15	20	15	10	5
Experiment#5 (S5)	15	20	25	15	5
Experiment#6 (S6)	15	20	25	10	0
Experiment#7 (S7)	20	10	25	10	0
Experiment#8 (S8)	20	10	25	15	5
Experiment#9 (S9)	20	10	15	10	5
Experiment#10 (S10)	20	20	25	15	0
Experiment#11 (S11)	20	20	15	10	0
Experiment#12 (S12)	20	20	15	15	5

3. Results

In this section, the obtained results are presented in four subsections. Surface roughness measurement and characterization of the Ti alloy samples before and after ECP, along with the obtained MRR, are documented in Section 3.1. In Section 3.2, the influence of AN is studied through surface characterization of samples that underwent AN following ECP. Section 3.3 provides a detailed analysis of the corrosion properties assessment of treated samples using electrochemical techniques. Finally, Section 3.4 presents the Taguchi analysis to study the influence of surface treatment factors and levels on roughness improvement, MRR, and corrosion resistivity.

3.1. Surface Texture Characterization and MRR Study after ECP

The bar graphs shown in **Figure 4** present the results of roughness measurements throughout the ECP process. For clarity, labels (S1, S2, S3,...) have been assigned to each designed experiment (see Table 2). In this study, the surface treatment considered in the DOE consists of two components: ECP and AN. ECP treatments were specifically conducted to improve surface quality. Therefore, Figure 4 depicts only the influence of ECP on the

surface texture parameters, the inclusion of the AN step is discussed in Sections 3.2 and 3.3.

As explained in the introduction, higher levels of the three selected factors in the DOE would accelerate or increase material removal. Such increase occurs by providing a higher level of driving force when a higher potential is applied, lowering viscosity and increasing ion solubility through a temperature increase, and extending the ECP duration to allow for more time for the reaction to occur. These hypotheses are supported by the observed results after ECP. In experiments #1 and #2 (performed on samples S1 and S2, respectively), where the factors were at their lowest levels, the roughness changes were minimal through all the studied texture parameters. The ECP treatments of these samples, resulted in average roughness parameter values of $\Delta S_a = 1.59\,\mu m$, $\Delta S_q = 4.46\,\mu m$, $\Delta S_z = 110.08\,\mu m$, and $\Delta S_{sk} = 0.7$.

Conversely, in experiment #10 (performed on sample S10), where the factors were at their highest levels, the roughness improvement was the most significant. The measured changes for surface texture parameters for this sample were $\Delta S_a = 7.72\,\mu m$, $\Delta S_q = 11.58\,\mu m$, $\Delta S_z = 168.60\,\mu m$, and $\Delta S_{sk} = 3.5$. However, some pit-like defects can be observed on the sample's surface, which are indicated by red dashed lines in **Figure 5**c. These pit defects specifically appeared in surface
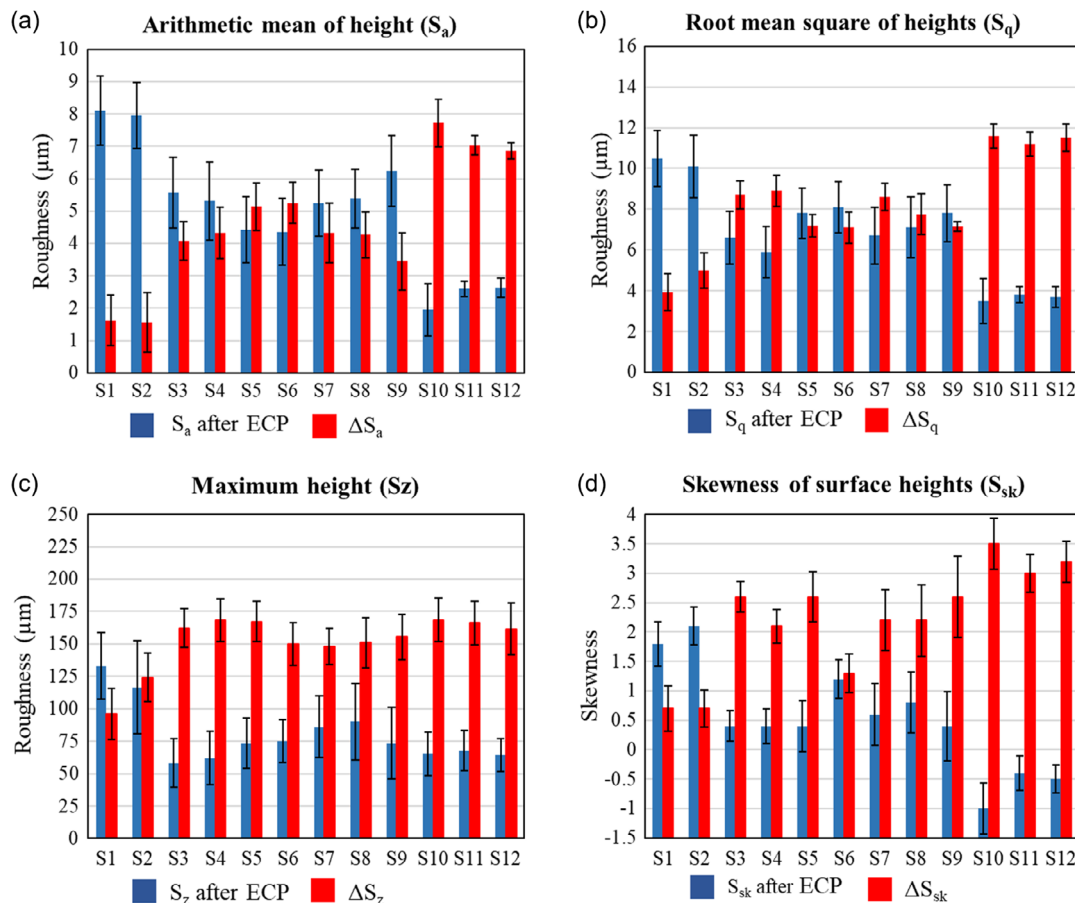

Figure 4. Stacked bar charts indicating the final values and changes in four surface texture parameters—a) S_a, b) S_q, c) S_z, and d) S_{sk}—resulting from the ECP process.
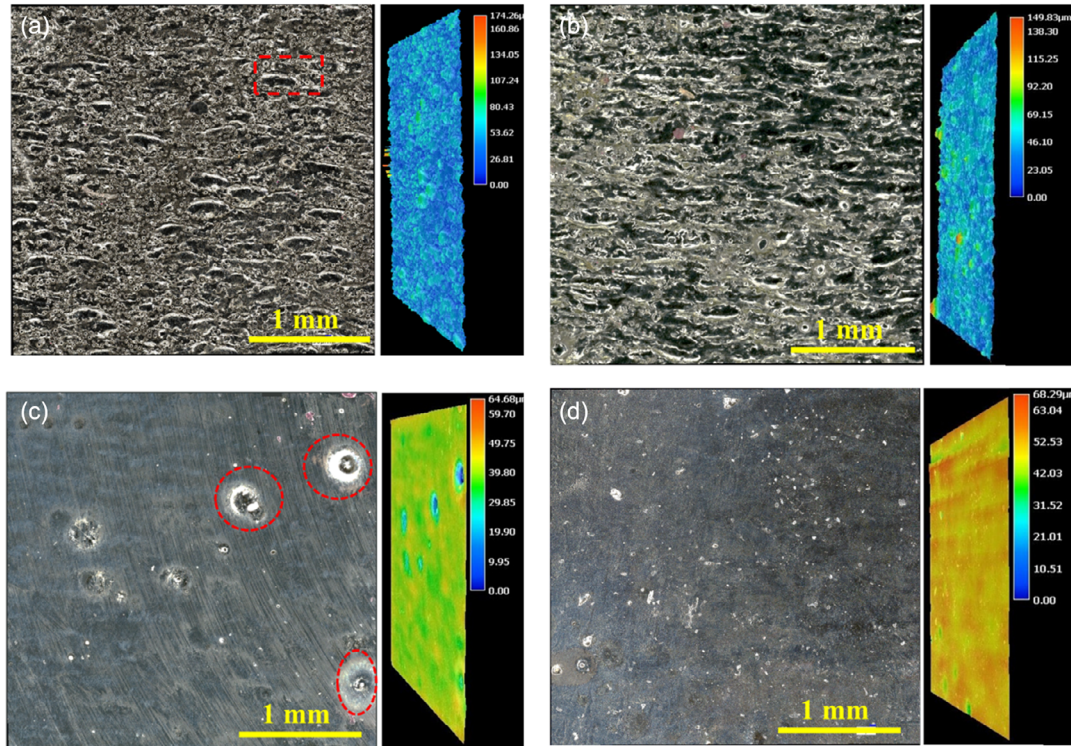
Figure 5. a) Surface topology of Ti–6Al–4V AM parts at AB condition and after ECP under different experimental conditions: b) 15 V, 10 min, 15 °C, c) 20 V, 20 min, 25 °C, and d) 20 V, 20 min, 15 °C. The red rectangle in (a) identifies the area shown in Figure 2c and the red circles in (c) show the pit-like defects.

roughness measurements as a negative S_{sk} value after ECP treatment. To be more specific, negative S_{sk} surface roughness values indicate a predominance of valleys on the surface, while positive values suggest a predominance of peaks.[60] Further, a more in-depth investigation into the effectiveness of each factor on surface roughness will be conducted using the Taguchi analysis discussed in Section 3.4.

Table 3 displays the MRR associated with each ECP treatment, which is considered as the treatment influencing material dissolution and roughness improvement. The MRR values in the ECP experiment range from 0.47 to 1.64 mg min^{-1}. To more comprehensively study, the influence of ECP factors on the MRR and ΔS, further Taguchi analysis was performed, and these results are elaborated in Section 3.4.

The samples' surface topology, obtained through digital microscopy, were investigated and are included in the Supporting Information section (Figure S1, Supporting Information) to maintain the conciseness of the text. However, the most relevant images for discussion are outlined in Figure 5. Figure 5a displays the surface topology, along with its color height map representing quantitatively the sample surface texture in its AB condition before any treatment. A randomly selected zone (indicated by a red rectangle in Figure 5a) of the AB rough surface at higher magnification is shown in Figure 2c, presenting irregularities in the flatness from layer to layer and semimelted particles attached to the surface.

In Figure 5b, when ECP is performed at 15 V and 15 °C for 10 min, the material removal was insufficient to provide a smooth surface. Some changes are visible, specifically in the upper-right area of the image, but it only resulted in a slight roughness reduction as quantitatively illustrated in Figure 4. This minor improvement might not be adequate for applications requiring a smooth finish.

Table 3. Mass loss and MRR during ECP process for each experiment.

Experiment	Δm [mg]	ECP time [min]	MRR of ECP [mg min^{-1}]
Experiment#1 (S1)	4.8 ± 1.6	10	0.48 ± 0.16
Experiment#2 (S2)	4.7 ± 1.9	10	0.47 ± 0.19
Experiment#3 (S3)	11.5 ± 2.3	10	1.15 ± 0.23
Experiment#4 (S4)	12.1 ± 1.6	20	0.60 ± 0.08
Experiment#5 (S5)	13.0 ± 2.5	20	0.65 ± 0.13
Experiment#6 (S6)	13.3 ± 2.1	20	0.66 ± 0.10
Experiment#7 (S7)	16.4 ± 2.3	10	1.64 ± 0.23
Experiment#8 (S8)	16.0 ± 2.9	10	1.60 ± 0.29
Experiment#9 (S9)	9.1 ± 2.4	10	0.91 ± 0.24
Experiment#10 (S10)	19.3 ± 2.1	20	0.96 ± 0.10
Experiment#11 (S11)	18.1 ± 3.6	20	0.90 ± 0.18
Experiment#12 (S12)	18.0 ± 3.1	20	0.90 ± 0.15

**ADVANCED
SCIENCE NEWS**

www.advancedsciencenews.com

**ADVANCED
ENGINEERING
MATERIALS**

www.aem-journal.com

Figure 5c shows the surface texture of sample S10, which involved high levels of the factors, resulting in a roughness value of $S_a = 1.95\,\mu m$, $S_q = 3.5\,\mu m$, $S_z = 65.4\,\mu m$, and $S_{sk} = -1$. The smooth surface becomes apparent when compared to the AB texture. To illustrate the effect of AN on a smooth surface obtained by ECP, the texture of sample S12, which underwent significant roughness reduction and was anodized according to the DOE table, is shown in Figure 5d. Although S10 achieved slightly better surface roughness based on S_a and S_q values, it was not anodized as part of the DOE plan. S12 was selected here, because it exhibited smoothness and AN was applied, allowing for a comparison of the surface texture before and after AN. Some pits are observable on the surface in Figure 5d (S12 samples); however, considering the color map height and S_{sk} value, they appear shallower than those in Figure 5c (S10 samples). By considering the visible colors around the pits on each color map and their corresponding values, the height values in Figure 5c (S10) range from dark blue to light orange (0–55 μm), while in Figure 5d (S12 sample), they range from green to orange (40–60 μm).

3.2. Surface Characterization after AN

Figure 6 depicts the surface morphologies of six samples after AN following the ECP process, as specified in the DOE (Table 2). The AN time, electrolyte, and temperature were kept constant across all samples, with the only variable being the AN potential. However, it is important to highlight that the previous ECP treatments applied to the samples differed significantly, as outlined in Table 2. These variations in ECP conditions led to different degrees of surface roughness improvement, as

discussed in Section 3.1. The impact of these different ECP treatments on surface roughness quality is further illustrated in the histograms (Figure 4) and macroscopic images (Figure 5). For experiments #3 (Figure 6a), #4 (Figure 6b), and #9 (Figure 6e), AN was carried out at $E = 10\,V$, while for experiments #5 (Figure 6c), #8 (Figure 6d), and #12 (Figure 6f), AN was conducted at $E = 15\,V$.

In Figure 6a,b, a "gold" colored oxide layer was formed uniformly on the surface. Similarly, Figure 6e depicts a "gold" colored oxide film on the surface, but including some brighter spots (highlighted by red squares), which seem to be due to localized breakdowns of the oxide film during AN. In Figure 6c,d, a "purple/blueish" colored oxide layer is evident on the surface, interspersed with bright-colored spots. These spots are the areas where the oxide layer has broken down, forming pits that exposed the base Ti–6Al–4V to the surface similar to those observed in Figure 6e but at a larger quantity. The sample depicted in Figure 6f features an oxide film with colors ranging from "gold" to "blue". The presence of pit defects is not detectable here.

Literature reports that the thickness of the anodic film increases with higher AN potential.[61–63] Additionally, the purple/blue[62] titanium oxide layer is known to be thicker than the oxide layer with a yellow/greenish[62] color. Taking into account these established facts and the observations in Figure 6, it can be concluded that AN at a higher potential of $E = 15\,V$ resulted in a thicker Ti oxide layer identified by a "blueish" color.

However, it was observed that AN at higher potential increased the pitting tendency. This can be attributed to the
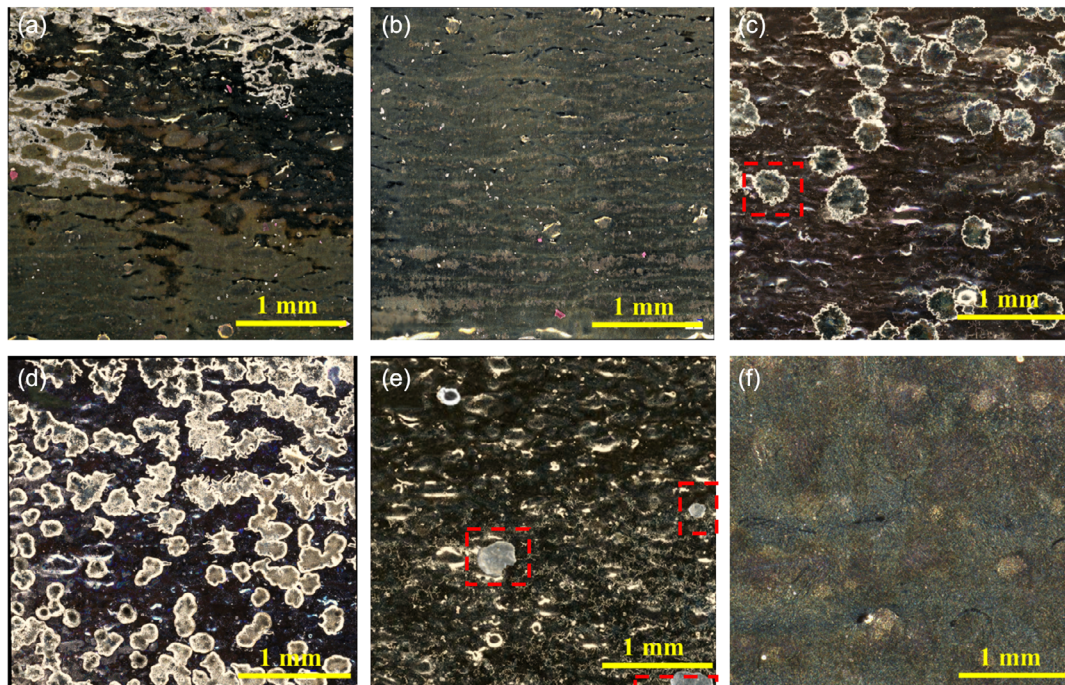

Figure 6. Surface topology of Ti–6Al–4V AM parts after ECP + AN at different experimental conditions: a) ECP: 15 V, 10 min, 25 °C and AN: 10 V, 5 min; b) ECP: 15 V, 20 min, 15 °C and AN: 10 V, 5 min; c) ECP: 15 V, 20 min, 25 °C and AN: 15 V, 5 min; d) ECP: 20 V, 10 min, 25 °C and AN: 15 V, 5 min; e) ECP: 20 V, 10 min, 15 °C and AN: 10 V, 5 min (red squares show the defect formed on surface); and f) ECP: 20 V, 20 min, 15 °C and AN: 15 V, 5 min.

**ADVANCED
SCIENCE NEWS**

www.advancedsciencenews.com

**ADVANCED
ENGINEERING
MATERIALS**

www.aem-journal.com

increased electrical energy provided by the higher potential difference and intensified electrochemical reactions. The pitting can be more pronounced when the surface texture is rougher (Figure 6c,d). Oppositely, in case of having a smooth surface prior AN like Figure 6f, can prevent the pit formation.

Figure 7a shows the confocal image of one the bright spots observed in sample S5 (as shown in Figure 6c by a red dashed square), serving as an example to indicate that these defects are actually deeper than the surrounding area and can be considered as pit defects. The maximum depth of this pit was documented as 23.45 μm and is shown in Figure 7b by a profile obtained by cross-sectioning the shown plane and the pit. Same characterizations were performed on sample S8 (Figure 6d) which had a rougher surface texture before AN. Random examination of pits revealed deeper pits up to 55 μm for this sample as is shown in Figure 7c,d, which could be associated with the rougher surface that promoted pit growth.

Using confocal microscopy, as shown in Figure 7, it became evident that the bright spots observed in Figure 5d and 6c are pit defects that were created specifically on rough surfaces while anodizing at higher potentials.[63] Conversely, AN at $E = 10$ V

resulted in an oxide layer which covered the surface uniformly (Figure 6a,b). Regarding the surface texture observed for S12, displayed in Figure 5f, it is evident that a smooth surface with an areal roughness value of $S_a = 3.15$ μm, $S_q = 3.30$ μm, $S_z = 47$ μm, $S_{sk} = -0.7$, contributed to a more uniform AN treatment and appeared to generate a more uniform oxide layer, even at the higher AN potential of $E = 15$ V. According to Figure 6e, it can be highlighted that even at lower AN potential a rough surface can cause pit formation.

3.3. Corrosion Evaluation

As mentioned in Section 2.3.3, for the corrosion evaluation, after recording the OCP value for 20 min, a linear polarization sweep from 0.4 V below OCP to +6.0 V versus OCP was applied. This potential range allowed to determine the corrosion potential and rate, as well as the passivation behavior and pitting corrosion on the samples. To assess the general corrosion behavior of the parts under study, the linear polarization curves around the OCP values are specifically assessed in **Figure 8** and the localized corrosion, which happens at higher potential ranges in the linear
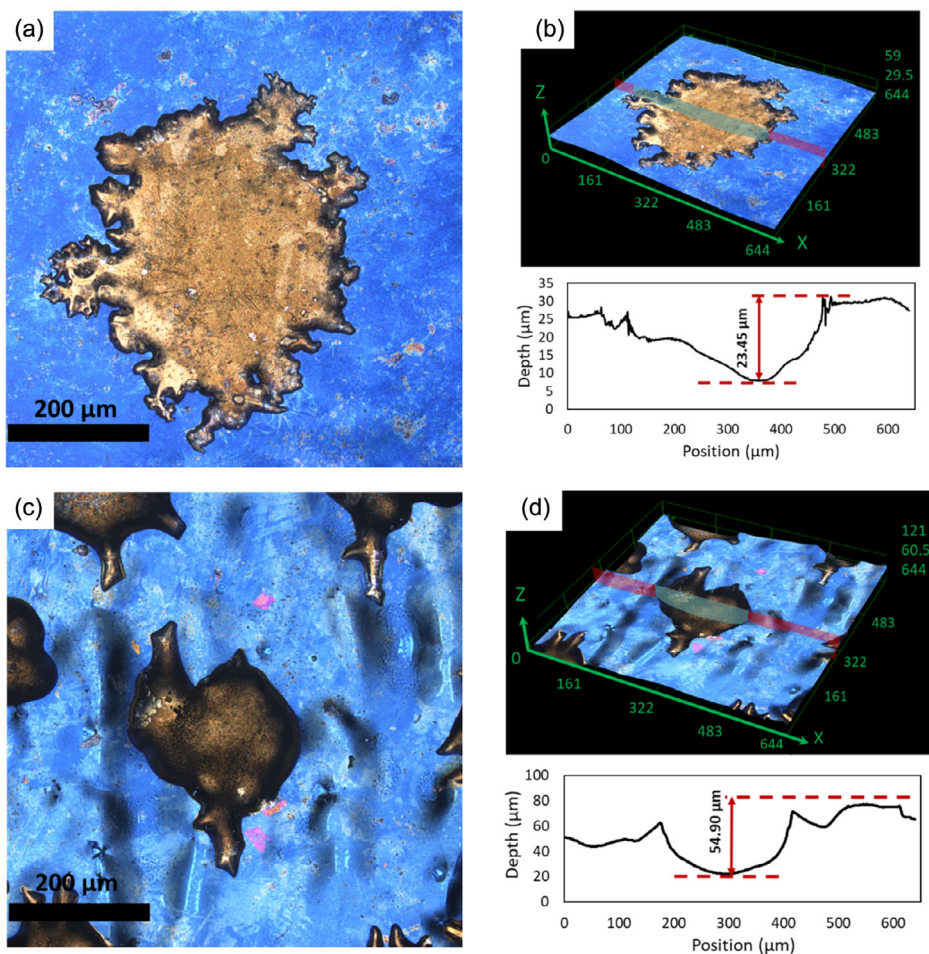

Figure 7. Confocal images of pits observed on anodized sample: a) 2D micrograph of sample S5 (ECP: 15 V, 20 min, 25 °C; AN: 15 V, 5 min), b) 3D micrograph and pit depth profile of sample S5, c) 2D micrograph of sample S8 (ECP: 20 V, 20 min, 25 °C; AN: 15 V, 5 min), and d) 3D micrograph and pit depth profile of sample S8.
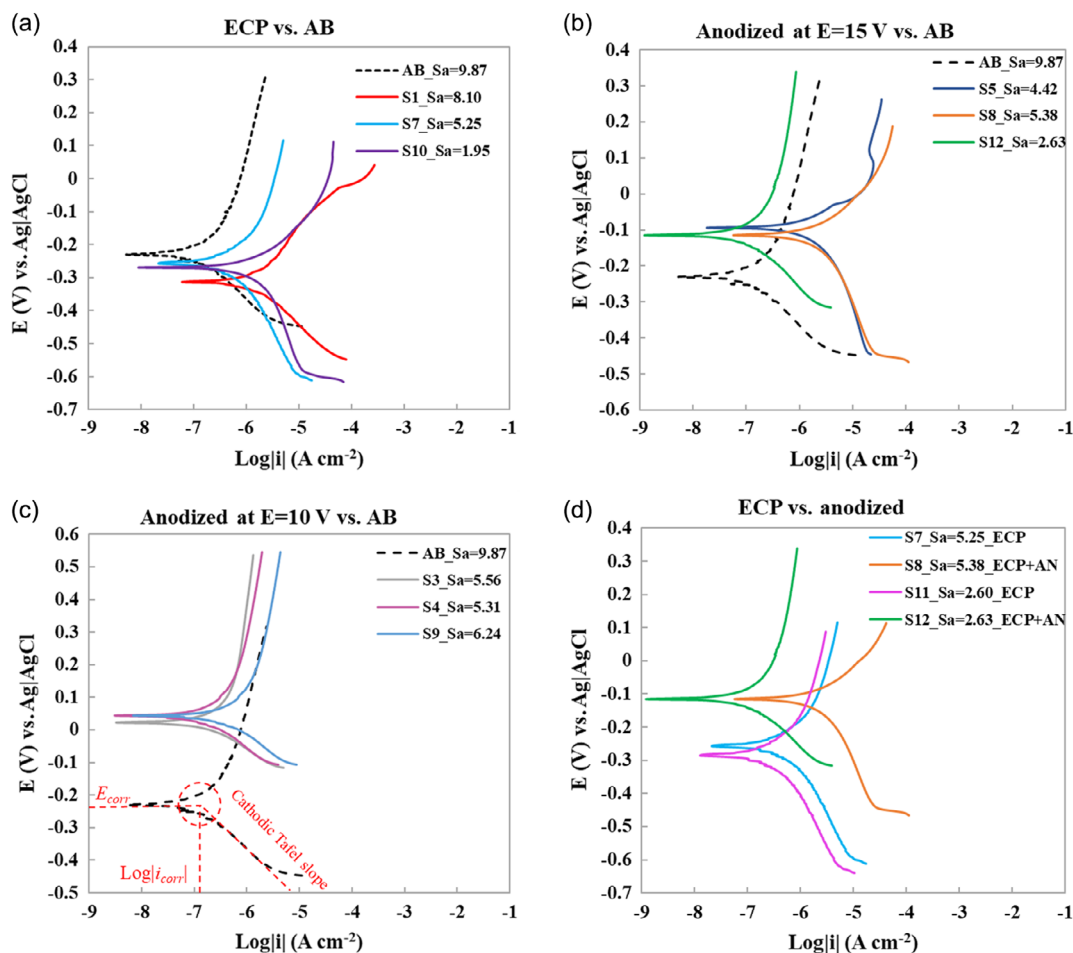
Figure 8. Polarization curves in the Tafel region for AM Ti–6Al–4V parts: comparison of E_{corr} and i_{corr} in a) AB parts and electropolished parts, b) ECP + anodized parts (AN) at $E = 5$ V and AB part, c) ECP + anodized parts at $E = 10$ V and AB part, and d) electropolished parts with ECP + anodized parts of the same roughness. All S_a values mentioned in the legend are in µm.

polarization tests, are evaluated in **Figure 9**. The final values describing the general and localized corrosion behavior are reported in **Table 4**. Based on preliminary experiments, the selected polarization sweep range will demonstrate the passivation and pitting of samples. However, this level of overpotential makes potentiodynamic polarization a destructive electrochemical corrosion evaluation method. Hence, it was not possible to perform a linear polarization test on a sample before and after treatment. Instead, linear polarization was applied to a separate sample in its AB condition as a reference.

Additionally, for experiments involving both ECP and AN treatment, linear polarization was conducted only after AN. The voltammograms of AM Ti–6Al–4V samples in AB condition and after selected treatment are depicted in Figure 8 and 9. The following thermodynamic corrosion parameters were obtained from analysis of voltammograms; (1) corrosion potential (E_{corr}) where anodic and cathodic branches intersect; (2) passivation potential (E_{pass}) where the current becomes constant due to the passivation; (3) pitting (breakdown) potential (E_{pit}) where a continuous increase of current is observed after the passivation region; and (4) pitting tendency ($|E_{corr} - E_{pit}|$), which shows the
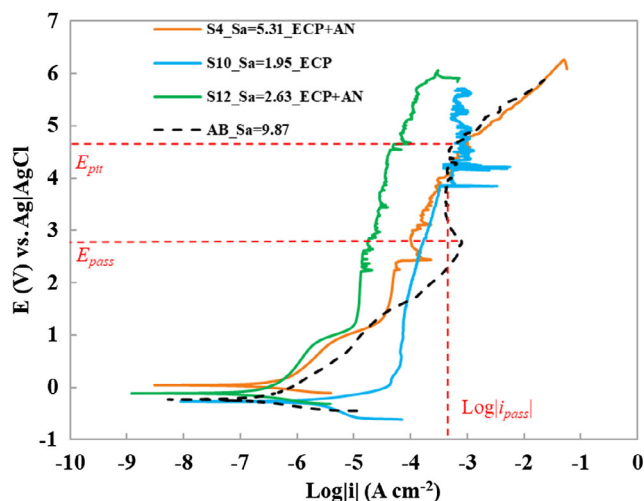

Figure 9. Potentiodynamic polarization of AM Ti–6Al–4V part in AB condition, after surface treatment #4 (ECP:15 V, 20 min, 15 °C and AN: 10 V, 5 min), after surface treatment #10 (20 V, 20 min, 25 °C), and after surface treatment #12 (ECP: 20 V, 20 min, 15 °C and AN: 15 V, 5 min).

Table 4. Thermodynamic and kinetic parameters obtained from potentiodynamic polarization of AM Ti–6Al–4V parts in AB condition and after surface treatments.

Part name	OCP [V]	E_{corr} [V]	E_{pass} [V]	E_{pit} [V]	$|E_{corr}-E_{pit}|$ [V]	i_{corr} [μA cm^{-2}]	$i_{pass} \times 10^{-4}$ [A cm^{-2}]
AB	-0.05 ± 0.02	-0.23 ± 0.10	2.73 ± 0.60	4.58 ± 0.40	4.81 ± 0.28	0.11 ± 0.08	6.40 ± 0.06
S1	-0.10 ± 0.04	-0.31 ± 0.15	0.63 ± 0.22	5.36 ± 0.33	5.67 ± 0.39	1.69 ± 0.12	9.81 ± 2.90
S2	-0.11 ± 0.03	-0.31 ± 0.18	1.17 ± 0.32	5.65 ± 0.20	5.96 ± 0.30	1.37 ± 0.10	16.0 ± 3.51
S3	0.23 ± 0.07	0.02 ± 0.12	1.43 ± 0.12	2.26 ± 0.33	2.24 ± 0.31	0.23 ± 0.04	0.18 ± 0.11
S4	0.18 ± 0.05	0.04 ± 0.08	1.48 ± 0.09	2.41 ± 0.25	2.37 ± 0.33	0.14 ± 0.07	0.48 ± 0.19
S5	-0.07 ± 0.08	-0.09 ± 0.13	1.27 ± 0.25	2.41 ± 0.41	2.50 ± 0.18	2.95 ± 0.11	1.88 ± 0.26
S6	-0.18 ± 0.08	-0.29 ± 0.09	0.42 ± 0.07	5.26 ± 0.51	5.50 ± 0.51	1.09 ± 0.09	6.18 ± 0.18
S7	-0.04 ± 0.05	-0.29 ± 0.17	1.12 ± 0.05	4.24 ± 0.48	4.53 ± 0.44	3.07 ± 0.08	6.96 ± 0.14
S8	-0.07 ± 0.07	-0.11 ± 0.12	1.36 ± 0.09	3.80 ± 0.26	3.91 ± 0.35	2.85 ± 0.22	5.23 ± 0.61
S9	0.21 ± 0.03	0.043 ± 0.07	1.39 ± 0.23	2.37 ± 0.25	2.33 ± 0.28	0.36 ± 0.13	1.05 ± 0.45
S10	-0.07 ± 0.06	-0.268 ± 0.05	0.41 ± 0.03	3.84 ± 0.31	4.11 ± 0.18	4.57 ± 0.71	1.56 ± 0.15
S11	-0.05 ± 0.07	-0.287 ± 0.1	1.12 ± 0.12	4.26 ± 0.61	4.54 ± 0.56	1.85 ± 0.33	4.18 ± 0.08
S12	0.08 ± 0.04	-0.115 ± 0.09	1.25 ± 0.19	5.69 ± 0.55	5.81 ± 0.42	0.09 ± 0.07	0.41 ± 0.05

susceptibility to pitting. Among the mentioned parameters, E_{pit} and $|E_{corr}-E_{pit}|$ are specifically used to compare the localized corrosion behavior of the parts.

In addition, several parameters describing corrosion kinetics were obtained from the cyclic potentiodynamic polarization graphs, such as; (a) corrosion current density (i_{corr}) where the anodic and cathodic Tafel slopes intersect, or in cases where there is not a well-defined anodic Tafel region, as observed in this study due to simultaneous dissolution and passivation reactions, the intersection of the cathodic Tafel slope and E_{corr} will be considered as i_{corr}; and (b) passive current density (i_{pass}), defined as the average of the current density in which the oxide film on the metal retains stable and protective and shows the performance of a passive film.[64]

These corrosion kinetics parameters are illustrated for the AB part in Figure 8c and 9 as an example; and the values for all samples were calculated using the obtained voltammograms; these results are summarized in Table 4. The standard deviations presented in the table were calculated based on three replicates for each sample. Figure 8 displays a limited potential range of the potentiodynamic polarization curves around OCP, i.e., at the Tafel region,[65] where the i_{corr} and E_{corr} values are calculated.

Figure 8a compares the polarization curves of the AB part with three ECP-treated parts that provided different areal roughness values. In this figure, it is evident that when only ECP is performed as the surface treatment, regardless of any roughness improvement, the E_{corr} value shifts toward a more negative potential. This observation indicates a higher thermodynamic tendency toward corrosion. Moreover, the current densities increase, signifying a higher corrosion rate. Both these observations show that ECP results in a decrease in corrosion resistivity of AM Ti–6Al–4V samples.

In Figure 8b, the voltammogram of the AB part is compared with samples that underwent AN at $E = 15$ V following ECP. The E_{corr} values for the combined ECP and AN treated parts are more positive than those for the AB parts. As for the i_{corr} values, they are higher for S5 and S8 but lower for S12 compared to the i_{corr} of

the AB part. This difference may be attributed to the lower surface roughness of the S12 part and the absence of pit defects formed during AN (see Section 3.2). The lowest achieved corrosion current density among all treated parts was obtained for S12, which was 0.09 ± 0.07 μA cm^{-2}. Considering the standard deviations of i_{corr} calculation, this value is lower than or similar to the i_{corr} of AB part, which was 0.11 ± 0.08 μA cm^{-2}. This suggests that by performing ECP followed by AN, surface roughness can be improved while maintaining the same or even better corrosion resistance as the AB part.

Figure 8c compares the voltammograms of the AB part with samples that were anodized at $E = 10$ V after the ECP treatment. It is evident that all AN-treated samples, following ECP, have larger E_{corr} values and similar or lower i_{corr} values compared to AB part. This observation shows that creation of a uniform oxide layer by AN at $E = 10$ V improved the corrosion behavior.

Finally, in Figure 8d, the effect of AN on corrosion properties is highlighted by comparing the voltammogram of parts that exhibit similar surface roughness values. One pair of them has undergone ECP only, while the other pair has been both electropolished and anodized. Parts S8 and S12 have the same roughness as parts S7 and S11, respectively. The E_{corr} values for S8 and S12 samples are more positive than those for S7 and S11, which were only electropolished. However, when comparing the i_{corr} values of S7 and S8, it is notable that despite the AN of S8, pit formation during AN led to a higher i_{corr} compared to S7. Conversely, in the case of S11 and S12, AN resulted in a more uniform oxide layer on a smoother surface, leading to decreased i_{corr} values. This demonstrates that employing suitable AN parameters to achieve a uniform oxide film on the surface can improve corrosion behavior. The rest of voltammograms in Tafel region are presented in Figure S2, Supporting Information.

Figure 9 shows the potentiodynamic voltammetry of selected samples over the full potential sweep range. In this figure, voltammograms of AM Ti–6Al–4V parts are presented under different conditions: at AB state, after treatment, S4 showing

the lowest i_{corr} among the samples anodized at $E = 10\,V$ with medium surface roughness improvement, after treatment, S10 presenting the lowest surface roughness, and after treatment S12, which involved combination of ECP and AN resulting in the second smoothest surface and the lowest i_{corr} value.

Indeed, Figure 9 clearly demonstrates that the treated parts exhibit different behavior in the higher potential ranges. As the overpotential increases in the anodic branch, the first noticeable difference appears in the starting passivation potential. Part S10 exhibits the lowest passivation potential, with a passive region initiating at 0.41 V and pitting starting at 3.84 V. For S4 the passive region begins 1.48 V and shows early breakdown at 2.41 V. For S12, the passive region begins at 1.25 V, and the part starts to develop some metastable pits at a potential of 2 V, while the breakdown potential, as reported in Table 4, was around 5.81 V. In contrast, the AB part experiences passivation at a higher potential (2.73 V), with pitting initiating at 4.58 V.

Additionally, besides these differences in E_{pass} and E_{pit} values, the most significant observation is the lower current density throughout the entire potential range for S12. This lower current density indicates a slower anodic reaction rate for this part at different potentials, making it a better option for corrosive environments. A complete overview of the potentiodynamic polarization curves is available in Figure S3, Supporting Information.

The occurrence of metastable pitting in Ti alloys has been reported in the literature[1] and can also be observed in our study. During the metastable state, there is a competitive process between dissolution and repassivation, which appears as fluctuations in the polarization curves. As the dissolution rate gradually increases, it may reach a critical condition, leading to the formation of stable pits.[66] This transition is observed as a sudden increase in current density in the polarization curves.

Regarding the sudden increase in current density during linear sweep voltammetry, it should be noted that oxygen evolution does occur within the potential range in this study.[67] However, this sudden current density increase cannot be solely attributed to oxygen evolution; it is indicative of the occurrence of pitting corrosion. This claim is supported by the postexperiment analysis of the samples following linear polarization experiments, where clear signs of pitting corrosion were observed. **Figure 10** further confirms the presence of pitting corrosion, showing SEM images of the AB sample after linear polarization. Figure 10a captures a low-magnification view of the surface, with a red box highlighting a pit. Figure 10b shows a higher magnification SEM image of the pit, providing a detailed view of the corrosion morphology.

3.4. Taguchi Analysis

Taguchi analysis is used to select the parameters that optimize surface treatment factors and levels, employing statistical methods to identify the most impactful variables on process outcomes. Main effect plots are created to visually represent the effects of factors. In **Figure 11**, the main effect plots display the mean values of S_a roughness changes at various factor levels. Among the
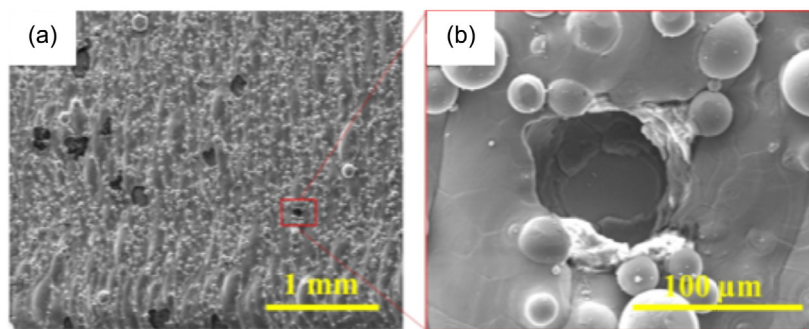

Figure 10. SEM images of pitting corrosion on the AB sample after linear polarization. a) Overview image of the corroded surface depicting numerous pits on the surface, b) higher magnification of one pit, indicated by the red box on (a).
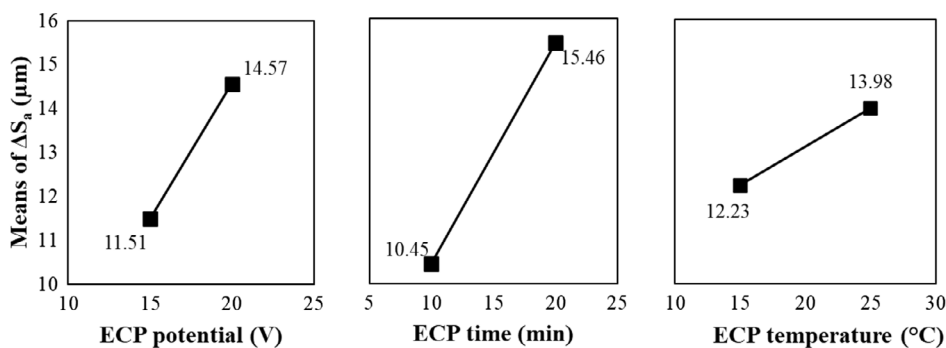

Figure 11. Main effect plots for mean of S_a roughness changes considering three ECP factors potential, time, and temperature.

various observed surface texture parameters in this study (see Section 3.1), the arithmetic mean areal roughness parameter S_a is selected due to its increased industry usage.[54] The interaction graphs reveal that ECP time exhibits the most significant variation in the vertical position of the plotted mean roughness improvement points, indicating that ECP duration has the most substantial influence on roughness improvement. ECP potential and ECP temperature are ranked as second and third important factors, respectively.

The main effect plots for MRR are displayed in **Figure 12**. These plots indicate that the ECP factors have a similar influence on MRR. However, when sorting them based on the differences in means at various factor levels, they can be ranked in the following order: ECP potential, ECP time, and ECP temperature. To explain the negative slope in the mean versus ECP time line, it is important to note that as the ECP duration increases, ion dissolution decreases exponentially, which causes the decrease in MRR. This phenomenon is a result of the mass-controlled nature of this process. In other words, although the overall material loss increases, the rate of material dissolution, or MRR, decreases.

To explore the influence of processing factors on i_{corr}, as a parameter to determine corrosion resistivity, both ECP and AN factors are considered in the main plots of **Figure 13**. Based on the plots, the most influential factor for corrosion rate is ECP temperature, with the lowest corrosion current density observed at lower ECP temperatures. The next significant factor is AN time, which, in this study, is having the AN step following the ECP treatment. Subsequently, the next influential factor is AN potential, with higher levels resulting in higher current

density. While the most corrosion-resistant sample (S12) was anodized at $E = 15$, the other samples that were anodized at the same potential displayed high i_{corr} and pitting defects. An increase in i_{corr} is detected by increasing the AN potential, as the plot displays the mean value. The last two influential factors are ECP potential and ECP time, respectively. These observations are further discussed in Discussion Section.

4. Discussion

In the Section 3, the results for surface roughness measurement, surface characterization, corrosion examination, and Taguchi analysis for different electrochemical surface treatments of PBF-LB-produced Ti–6AL–4V samples were reported separately. Now, in this section, the relation between the obtained results and observations will be discussed. In this study, the DOE considered two postprocessing treatments: ECP and AN. For ECP, three factors were taken into account: ECP potential, time, and temperature. For AN, two factors were considered: AN potential and time. Each factor included two levels. All factor levels, based on the Taguchi L12 orthogonal array, are presented in Table 2 (Section 2.4). The aim was to treat half of the samples with ECP alone and the other half with both ECP and AN to study the distinct effects of ECP and ECP combined with AN. Consequently, two levels of AN time were considered: 0 and 5 min. Experiments including 0 min AN time indicated that no AN was applied, and the sample was solely electropolished.

After surface treatment, the initial focus was on comparing the change in surface roughness parameters (ΔS_a, ΔS_q, ΔS_z, and
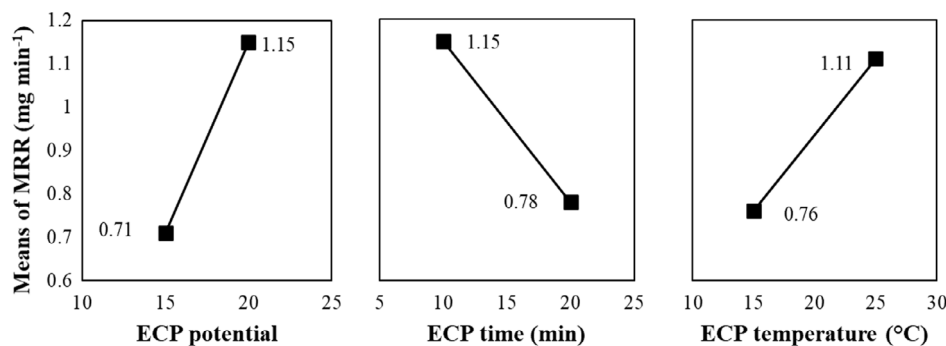

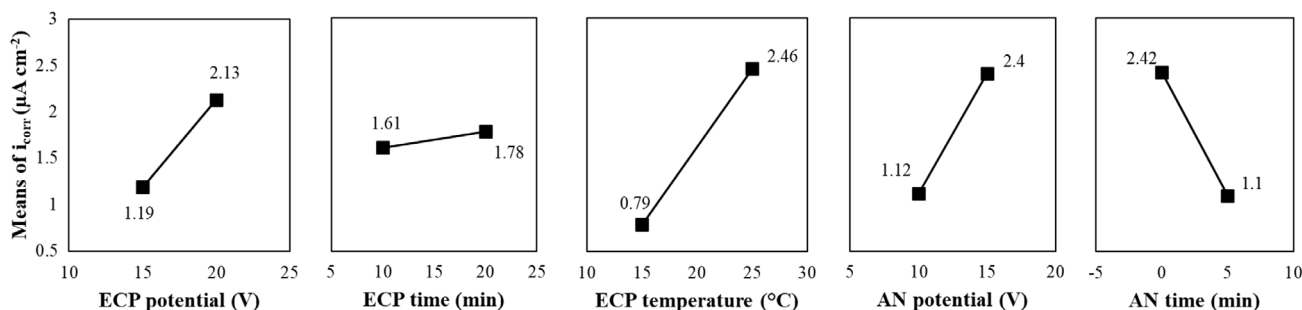**Figure 12.** Main effect plots for mean of MRR considering three ECP factors potential, time, and temperatures.

Figure 13. Main effect plots for mean of corrosion current densities considering all five factors included in the DOE.

ADVANCED
SCIENCE NEWS

www.advancedsciencenews.com

ADVANCED
ENGINEERING
MATERIALS

www.aem-journal.com

ΔS_{sk}) under various experimental conditions. Further examination of each sample's surface roughness before and after the ECP experiment led to the conclusion that experiment S10 demonstrated the most significant roughness changes, $\approx\Delta S_a = 7.72\,\mu m$, $\Delta S_q = 11.58\,\mu m$, $\Delta S_z = 168.60\,\mu m$, and $\Delta S_{sk} = 3.5$. In this experiment, the ECP factors potential, time, and temperature were at their highest levels, with values of 20 V, 20 min, and 25 °C, respectively. This observation aligns with the theoretical understanding of material dissolution and ion diffusion in the ECP process. In theory, higher overpotential, longer process duration, and higher temperature can either accelerate metal oxidation and dissolution or increase the total amount of material loss. This increased material dissolution ultimately leads to a smoother surface finish.[34,35,68]

In contrast, experiments S1 and S2 (Table 2) were performed at the lowest levels of ECP potential, time, and temperature, which resulted in the lowest roughness changes of around $\Delta S_a = 1.59\,\mu m$, $\Delta S_q = 4.46\,\mu m$, $\Delta S_z = 110.08\,\mu m$, and $\Delta S_{sk} = 0.7$. The influence of ECP factors on roughness changes, for different process conditions, was further discussed in Section 3.4. The main effect plots of S_a roughness changes mean values, revealed that ECP time is the most influential factor for improving roughness through the ECP process, followed by ECP potential. ECP temperature was found to have the least effect.

Regarding the MRR, experiment S7, in which ECP was performed at a higher potential (20 V) and temperature (25 °C) and a lower level of time (10 min), achieved the highest MRR value of $1.64\,mg\,min^{-1}$. In contrast, experiments S1 and S2, which were performed at lower levels of potential (15 V) and temperature (15 °C) and a lower level of time (10 min), had the lowest MRR value of $0.47\,mg\,min^{-1}$ among all the experiments.

Based on Figure 12, the main effect plots of the average MRR values at different factor levels, it is observed that the three ECP processing factors, namely, potential, time, and temperature, have nearly equal influence on MRR. However, the influence slope of the plot for the factor time is negative. This indicates that, for the same levels of ECP potential and temperature, increasing the ECP time results in a decrease in MRR. It is important to note that this decrease does not imply a reduction in the total material removal; instead, it signifies a decrease in the rate of material removal due to the role of time in the MRR equation (Equation 3).

The corrosion behavior of the samples after the treatments was assessed using potentiodynamic voltammetry to compare them to the AB part. It was observed that the parts that underwent only ECP had lower E_{corr} values, indicating a higher susceptibility to corrosion. Additionally, for these samples, the corrosion density increased compared to the nontreated part, demonstrating a higher degradation rate in corrosive conditions, such as saline environments. This observation can be attributed to the removal of the natural passive layer and the prevention of TiO_2 formation on the surface of the parts treated with ECP.

In this study, the electrolyte contains 20 vol% ethanol, which reacts with the $TiCl_4$ film stacked on the parts, dissolving it into the electrolyte. This reaction prevents the trace of H_2O, available in the ethylene glycol-based electrolyte, from reacting with $TiCl_4$ to form TiO_2.[39] Consequently, this process helps achieving a shiny surface on Ti alloy parts through ECP. However, not having the protective passive film on the treated Ti–6Al–4V parts

resulted in a diminished corrosion behavior. According to the results of this study, AN treatment can address this issue and enhance the corrosion behavior of metallic samples.

To more specifically address this aspect, conducting an treatment on Ti alloy AM samples, subsequent to ECP, that does not form a protective passive film, proves to be effective. This sequence allows for the formation of a robust passive film, after the surface roughness reduction step by ECP, significantly enhancing the corrosion resistance of Ti–6Al–4V parts. This finding represents a novel contribution of our study for the research community, highlighting an effective strategy for improving the durability of these alloy components after ECP.

This successful postprocessing strategy becomes evident from the voltammograms of the samples that underwent both ECP and AN, as shown in Figure 8b,c. The E_{corr} values for all of them were more positive than the E_{corr} of the AB, nontreated part. Additionally, under the AN condition in which the oxide film covered the entire surface and no pits were formed during AN, a lower corrosion current density was observed, indicating superior corrosion behavior compared to the AB part. This uniform oxide film was achieved when the AN potential was at its highest level (15 V) and the surface roughness was reduced by ECP down to $S_a = 2.63\,\mu m$. As shown in Figure 4, this treatment led to the second smoothest surface, with a 72% improvement in S_a roughness. Following the ECP treatment, the sample underwent AN, which, according to Table 4 and Figure 8 and 9, resulted in the best corrosion behavior, characterized by the lowest corrosion current density, the highest pitting potential, and the lowest pitting tendency.

At higher potential ranges, the voltammograms were compared, and E_{pass}, E_{pit}, and i_{pass} values were reported in Table 4. Additionally, the most significant observation from the voltammograms of Figure 9 at higher potentials (1.0–6.0 V) was the consistently lower current density for sample S12. Indeed, this sample (S12), which was anodized under conditions that produced a uniform oxide layer and that had been previously smoothed by ECP, showed these characteristics across the entire potential range.

The main effect plots were analyzed to identify the parameters that most significantly influence the i_{corr} values. Based on the plots, the most influential factor for corrosion rate is the ECP temperature. Among all ECP-treated samples, samples that were electropolished at $T = 15\,°C$ had the lowest corrosion rate. The next significant factor is AN time, which, in this study, determined if either the AN step, post-ECP, was applied or not. The next influential factor is AN potential, with higher levels resulting in lower current density.

The two least influential factors are ECP potential and ECP time, respectively. To explain the importance of temperature on ECP, it should be noted that according to the literature, ECP at lower temperature is beneficial due to decreasing the current density and expansion of steady state current density plateau in anodic polarization curves.[69,70] Lower current density leads to smoother and more uniform material dissolution during ECP.

The metallic alloy parts used in this study were produced by AM (PBF-LB) and observation of nonuniform material dissolution at higher temperature is difficult, because of their heterogeneity in surface texture. However, for experiment S10 which resulted in a smoother surface (see Figure 5c), a localized

**ADVANCED
SCIENCE NEWS**

www.advancedsciencenews.com

**ADVANCED
ENGINEERING
MATERIALS**

www.aem-journal.com

material dissolution can be observed. This might be due to over-electropolishing that was also observed in literature, when conducting ECP at higher temperatures.[34]

Over-polishing of the surface can hinder its corrosion resistance because pit-like areas make the surface more susceptible to degradation, resulting in a higher i_{corr}. In the performed Taguchi analysis, AN time and potential are ranked as the second and third most influential factors in the i_{corr} of the treated parts. As expected, and as shown in Figure 6, the AN step created an oxide film on the surface of the parts. Performing AN at higher potential led to the creation of a more uniform and thicker 'yellow/greenish' colored oxide film on the AM part.

Based on the experiments and analysis conducted in this study to select the best postprocessing experimental condition within the scope of the factors and levels considered, the following recommendations can be presented: 1) To achieve a significant improvement in surface roughness, it is recommended to use the ECP method described in experiment S10, which resulted in a 7.72 μm reduction in S_a surface roughness, equivalent to an improvement of 80% compared to the AB parts. In this experiment, ECP was conducted at a potential of 20 V and a temperature of 25 °C for a duration of 20 min. 2) To achieve a smooth surface with corrosion resistance similar to or better than the AB part, it is essential to include an AN treatment. If the ECP step results in a smooth surface with a S_a value of 2.63 μm, reflecting a 72% improvement as seen in experiment S12, applying AN at $E = 15$ V for 5 min can generate a uniform oxide film on the surface. However, if the surface is not sufficiently smooth (S_a exceeding 4 μm, as observed in this study), it is recommended to decrease the AN potential to $E = 10$ V to create a more uniform on a rough surface.

To summarize the key findings of this study, the comparative process flowchart depicted in **Figure 14** introduces the surface state and corrosion behavior of the AB AM Ti-alloy part shown in the dashed frame, followed by the experimental processes that yield the maximum roughness improvement (ECP) or the best corrosion resistivity (ECP + AN), and the obtained process-specific characterization parameters after treatment. The achieved arithmetic areal surface roughness of 2.63 μm and corrosion current density of 0.09 μA cm^{-2} demonstrate significant improvements compared to the original AB part, which had a surface roughness of 9.49 μm and a corrosion current density of 0.11 ± 0.08 μA cm^{-2}. The 72% reduction in surface roughness highlights the effectiveness of the ECP treatment in significantly improving the surface finish. The subsequent AN treatment, applied after ECP, plays a critical role in reducing the corrosion rate. As shown in Table 4, the sample with a similar roughness (S11) but no post-AN step revealed a corrosion current density of 1.85 μA cm^{-2}, which is twice as large compared to the anodized S12 sample. Indeed, the lower corrosion current density post-AN treatment (e.g., S12) reflects a significant decrease in the material's susceptibility to corrosion, i.e., enhanced corrosion resistance. These substantial improvements in both surface quality and corrosion performance validate the success of the postprocessing treatments in meeting their intended objectives.

In fact, the developed flowchart (Figure 12) can be employed as a decision support tool for academic or industrial researchers aiming to identify the best routes to follow for AB AM Ti–6Al–4V parts postprocessing strategies. Indeed, if the goal is to achieve a smooth surface, and corrosion properties are less important, the blue arrows should be followed. If the corrosion properties of the postprocessed part are important, the green arrows should be followed. This path also results in reasonably good surface finishing.
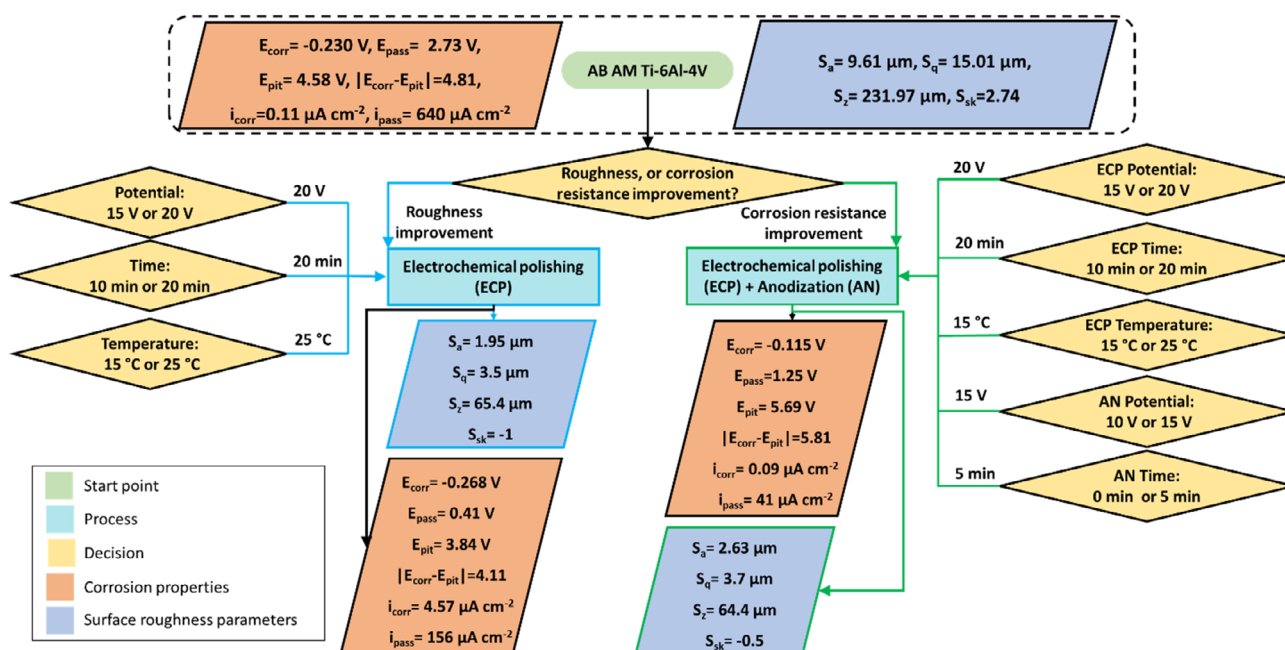

Figure 14. Comparative flowchart of ECP and ECP + AN postprocessing, summarizing key results, and outlining the optimal paths for achieving the best corrosion properties and surface finishing.

5. Conclusion

The present study employed a DOE approach using an L12 orthogonal array to optimize the postprocessing of AM Ti–6Al–4V parts. In the DOE, two surface treatments, ECP and AN, were considered. For ECP, factors such as potential, temperature, and time were considered, while AN involved factors of time and potential, all including two levels. The surface roughness of the samples and their weight were measured both before and after each treatment to determine, respectively, the optimal experimental conditions that yield the highest roughness improvement and the fastest MRR. Additionally, the corrosion behavior of the treated samples was examined using the potentiodynamic linear polarization technique to assess the impact of the surface treatment conditions on their corrosion resistance. A Taguchi analysis was performed to determine the surface treatment factors that have the most significant influence on the studied process performance parameters, including roughness improvement, MRR, and corrosion rates. Based on the obtained results, the following conclusions can be made: 1) ECP at $E = 20$ V, $T = 25$ °C, for 20 min resulted in the highest roughness improvement of $\Delta S_a = 80\%$ and the smoothest surface achieving $S_a = 1.95$ μm. However, some pit-like surface defects were visible on the electropolished surface, indicating over-electropolishing. Another ECP condition with similar parameters, but performed at a decreased processing temperature of 15 °C achieved a surface roughness of $S_a = 2.60$ μm with no such surface defects. Therefore, the latter processing condition is preferable. 2) The ECP experiment with the highest MRR was conducted at a high potential of $E = 20$ V and a high temperature of $T = 25$ °C for 10 min. This can be explained by the fact that the ECP process is controlled by the diffusion of ions into the solution, and over time, the amount of material being dissolved will exponentially decrease. As a result, the MRR is higher in its initial stages compared to the later stages. 3) Corrosion behavior of the electrochemically treated parts is affected by postprocessing. ECP treatments increased both the E_{corr} and i_{corr} of the parts compared to its AB surface, which shows inferior corrosion resistance. However, it was proven that by applying a proper AN treatment following ECP, a protective oxide layer can be formed on the surface to improve the corrosion resistance. The best corrosion behavior was measured for a Ti–6Al–4V alloy part electropolished at $E = 20$ V, $T = 15$ °C, for 20 min and further anodized at $E = 15$ V for 5 min. In addition, considering the current density across the entire range of potential scan and its passive behavior, it is selected as the most favorable for corrosion properties. 4) The most influential factors for the postprocessing conditions were identified through Taguchi analysis using main effect plots. For roughness improvement, ECP time, potential, and temperature respectively influenced the process. In terms of MRR, the plots indicate that the ECP factors have relatively similar influences. When considering corrosion rate (i_{corr} values as a criterion), the three most influential factors are ECP temperature, AN time, and AN potential, respectively. 5) The combined treatment of ECP at 20 V and 15 °C for 20 min followed by AN at 15 V for 5 min on AB LB-PBF fabricated Ti–6Al–4V parts was identified as the optimal condition for achieving both significant surface smoothness (72% S_a roughness improvement) and enhanced corrosion resistance. This outcome, supported by both surface roughness and electrochemical measurements, highlights the importance of integrating ECP and AN for improved performance and is among the key findings of this study.

Based on the results of this study, ECP and AN in an eco-friendly solution composed of NaCl and ethylene glycol, with the addition of ethanol/water, can be successfully used to improve surface roughness and corrosion behavior of AM Ti–6Al–4V surfaces.

Supporting Information

Supporting Information is available from the Wiley Online Library or from the author.

Conflict of Interest

The authors declare no conflict of interest.

Author Contributions

Shamim Pourrahimi: Formal analysis (lead); Investigation (lead); Methodology (lead); Visualization (lead); Writing—original draft (lead); Writing—review and editing (equal). **Lucas A. Hof**: Methodology (equal); Project administration (lead); Resources (lead); Supervision (lead); Writing—review and editing (lead).

Data Availability Statement

The data that support the findings of this study are available in the supplementary material of this article.

[1] Y. W. Cui, L. Y. Chen, P. Qin, R. Li, Q. Zang, J. Peng, L. Zhang, S. Lu, L. Wang, L. C. Zhang, *Corros. Sci.* **2022**, *203*, 110333.

[2] W. D. Brewer, R. K. Bird, T. A. Wallace, *Mater. Sci. Eng.: A* **1998**, *243*, 299.

[3] I. Gurrappa, *Mater. Charact.* **2003**, *51*, 131.

[4] N. Dai, L. C. Zhang, J. Zhang, Q. Chen, M. Wu, *Corros. Sci.* **2016**, *102*, 484.

[5] P. Tyagi, T. Goulet, C. Riso, R. Stephenson, N. Chuenprateep, J. Schlitzer, C. Benton, F. Garcia-Moreno, *Addit. Manuf.* **2019**, *25*, 32.

[6] K. Karami, A. Blok, L. Weber, S. M. Ahmadi, R. Petrov, K. Nikolic, E. V. Borisov, C. Leeflang, C. Ayas, A. A. Zadpoor, M. Mehdipour, E. Reinton, V. A. Popovich, *Addit. Manuf.* **2020**, *36*, 101433.

[7] J. Guo, K. H. Au, C. N. Sun, M. H. Goh, C. W. Kum, K. Liu, J. Wei, H. Suzuki, R. Kang, *J. Mater. Process. Technol.* **2019**, *264*, 422.

[8] A. P. Nagalingam, S. H. Yeo, *Wear* **2018**, *414–415*, 89.

[9] L. Y. Chen, S. X. Liang, Y. Liu, L. C. Zhang, *Mater. Sci. Eng. R: Rep.* **2021**, *146*, 100648.

[10] S. Chowdhury, N. Yadaiah, C. Prakash, S. Ramakrishna, S. Dixit, L. R. Gupta, D. Buddhi, *J. Mater. Res. Technol.* **2022**, *20*, 2109.

[11] W. J. Sames, F. A. List, S. Pannala, R. R. Dehoff, S. S. Babu, *Int. Mater. Rev.* **2016**, *61*, 315.

[12] E. Maleki, S. Bagherifard, M. Bandini, M. Guagliano, *Addit. Manuf.* **2021**, *37*, 101619.

[13] T. M. Mower, M. J. Long, *Mater. Sci. Eng. A* **2016**, *651*, 198.

[14] F. Cabanettes, A. Joubert, G. Chardon, V. Dumas, J. Rech, C. Grosjean, Z. Dimkovski, *Precis. Eng.* **2018**, *52*, 249.

[15] L.-Y. Chen, P. Qin, L. Zhang, L.-C. Zhang, L.-Y. Chen, P. Qin, L. Zhang, L.-C. Zhang, *Int. J. Extreme Manuf.* **2024**, *6*, 052006.

[16] J. Hartcher-O'Brien, J. Evers, E. Tempelman, *Mater. Today Commun.* **2019**, *19*, 300.

[17] F. Svahn, Å. Kassman-Rudolphi, E. Wallén, *Wear* **2003**, *254*, 1092.

[18] D. Arola, C. L. Williams, *Int. J. Fatigue* **2002**, *24*, 923.

[19] W. Li, D. Y. Li, *Acta Mater.* **2006**, *54*, 445.

[20] N. Mohammadian, S. Turenne, V. Brailovski, *J. Mater. Process. Technol.* **2018**, *252*, 728.

[21] S. Han, F. Salvatore, J. Rech, J. Bajolet, *Precis. Eng.* **2020**, *64*, 20.

[22] M. Sayuti, F. Yusof, Y. Dambatta, *J. Test Eval.* **2018**, *46*, 1673.

[23] J. Delgado, J. Ciurana, C. A. Rodríguez, *Int. J. Adv. Manuf. Technol.* **2011**, *60*, 601.

[24] S. Pourrahimi, L. A. Hof, *Adv. Eng. Mater.* **2024**, *26*, 2301511.

[25] P. B. Tailor, A. Agrawal, S. S. Joshi, *Int. J. Mach. Tools Manuf.* **2013**, *66*, 15.

[26] Z. Chaghazardi, L. Hof, R. Wuthrich, *ECS Trans.* **2020**, *97*, 523.

[27] ASTM B374-06, *Standard Terminology Relating to Electroplating* **2019**.

[28] D. Landolt, *Electrochim. Acta* **1987**, *32*, 1.

[29] S. Pourrahimi, L. Hof, *ECS Meeting Abstracts* **2022**, MA2022-01, 1217.

[30] J. Mu, T. Sun, C. L. A. Leung, J. P. Oliveira, Y. Wu, H. Wang, H. Wang, *Prog. Mater. Sci.* **2023**, *136*, 101109.

[31] W. Han, F. Fang, *Int. J. Mach. Tools Manuf.* **2019**, *139*, 1.

[32] C.-N. Kuo, Y.-C. Wu, C.-H. Ng, Y.-C. Chung, J. C. Huang, *Materials* **2019**, *12*, 1466.

[33] K. Alrbaey, D. I. Wimpenny, A. A. Al-Barzinjy, A. Moroz, *J. Mater. Eng. Perform.* **2016**, *25*, 2836.

[34] P. Lochyński, S. Charazińska, E. Łyczkowska-Widłak, A. Sikora, *Metals* **2019**, *9*, 1.

[35] M. Haïdopoulos, S. Turgeon, C. Sarra-Bournet, G. Laroche, D. Mantovani, *J. Mater. Sci. Mater. Med.* **2006**, *17*, 647.

[36] Y. Zhang, J. Li, S. Che, Y. Tian, *Met. Mater. Int.* **2020**, *26*, 783.

[37] M. B. García-Blanco, M. Díaz-Fuentes, O. Garrido, G. Vara, J. A. Díez, in *Proc. Euro PM 2015: Int. Power Metallurgy Congress and Exhibition*, The European Powder Metallurgy Association (EPMA), Brussels, Belgium **2015**.

[38] A. Kuhn, *Met. Finish.* **2004**, *102*, 80.

[39] D. Kim, K. Son, D. Sung, Y. Kim, W. Chung, *Corros. Sci.* **2015**, *98*, 494.

[40] G. S. Prihandana, T. Sriani, M. F. Jamaludin, F. Yusof, B. Arifvianto, M. Mahardika, *Metals* **2023**, *13*, 392.

[41] S. Yan, G. L. Song, Z. Li, H. Wang, D. Zheng, F. Cao, M. Horynova, M. S. Dargusch, L. Zhou, *J. Mater. Sci. Technol.* **2018**, *34*, 421.

[42] J. E. G. González, J. C. Mirza-Rosca, *J. Electroanal. Chem.* **1999**, *471*, 109.

[43] S. Hakimian, A. H. Bouzid, L. A. Hof, *J. Adv. Join. Process.* **2024**, *9*, 100200.

[44] M. İzmir, B. Ercan, *Front. Chem. Sci. Eng.* **2019**, *13*, 28.

[45] A. L. Martinez, D. O. Flamini, S. B. Saidman, *Trans. Nonferrous Met. Soc. China* **2022**, *32*, 1896.

[46] K. Fushimi, H. Habazaki, *Electrochim. Acta* **2008**, *53*, 3371.

[47] Q. A. Nguyen, Y. V. Bhargava, T. M. Devine, *Electrochem. Commun.* **2008**, *10*, 471.

[48] O. Rodríguez-Martínez, L. M. Martínez, M. Videa, *J. Nanopart. Res.* **2020**, *22*, 1.

[49] ASTM F136-13, *Standard Specification for Wrought Titanium-6Aluminum-4Vanadium ELI (Extra Low Interstitial) Alloy for Surgical Implant Applications (UNS R56401)* **2021**.

[50] M. M. Osman, *Mater. Chem. Phys.* **2001**, *71*, 12.

[51] G. Pyka, A. Burakowski, G. Kerckhofs, M. Moesen, S. Van Bael, J. Schrooten, M. Wevers, *Adv. Eng. Mater.* **2012**, *14*, 363.

[52] G. Dong, J. Marleau-Finley, Y. F. Zhao, *Int. J. Adv. Manuf. Technol.* **2019**, *104*, 3401.

[53] G. Pyka, G. Kerckhofs, I. Papantoniou, M. Speirs, J. Schrooten, M. Wevers, *Materials* **2013**, *6*, 4737.

[54] A. Acquesta, T. Monetta, *Metals* **2023**, *13*, 874.

[55] ASTM F3624-23, *Standard Guide for Additive Manufacturing of Metals - Powder Bed Fusion - Measurement and Characterization of Surface Texture* **2023**.

[56] ASTM G5-14, *Standard Reference Test Method for Making Potentiodynamic Anodic Polarization Measurements* **2021**.

[57] J. Antony, in *Design of Experiments for Engineers and Scientists*, Elsevier Ltd, Amsterdam **2003**.

[58] F. C. Tsai, B. H. Yan, C. Y. Kuan, F. Y. Huang, *Int. J. Mach. Tools Manuf.* **2008**, *48*, 932.

[59] R. K. Roy, *A Primer on the Taguchi Method*, Society of Manufacturing Engineers, Dearborn, Michigan **1990**.

[60] ISO 25178-2, *Geometrical Product Specifications (GPS) Surface Texture: Areal, Part 2: Terms, Definitions and Surface Texture Parameters* **2021**.

[61] A. Pérez del Pino, J. M. Fernández-Pradas, P. Serra, J. L. Morenza, *Surf. Coat. Technol.* **2004**, *187*, 106.

[62] M. V. Diamanti, B. Del Curto, M. P. Pedeferri, *Color Res. Appl.* **2008**, *33*, 221.

[63] A. Karambakhsh, A. Afshar, S. Ghahramani, P. Malekinejad, *J. Mater. Eng. Perform.* **2011**, *20*, 1690.

[64] Y. Bai, X. Gai, S. Li, L. C. Zhang, Y. Liu, Y. Hao, X. Zhang, R. Yang, Y. Gao, *Corros. Sci.* **2017**, *123*, 289.

[65] D. Li, C. Lin, C. Batchelor-McAuley, L. Chen, R. G. Compton, *J. Electroanal. Chem.* **2018**, *826*, 117.

[66] Y. Tang, Y. Zuo, J. Wang, X. Zhao, B. Niu, B. Lin, *Corros. Sci.* **2014**, *80*, 111.

[67] A. Hemmasian Ettefagh, C. Zeng, S. Guo, J. Raush, *Addit. Manuf.* **2019**, *28*, 252.

[68] S. Chang, A. Liu, C. Y. A. Ong, L. Zhang, X. Huang, Y. H. Tan, L. Zhao, L. Li, J. Ding, *Mater. Res. Lett.* **2019**, *7*, 282.

[69] P. Barnes, A. Savva, K. Dixon, H. Bull, L. Rill, D. Karsann, S. Croft, J. Schimpf, H. Xiong, *Surf. Coat. Technol.* **2018**, *347*, 150.

[70] O. Piotrowski, C. Madore, D. Landolt, *J. Electrochem. Soc.* **1998**, *145*, 2362.